

Overview of Alcator C-Mod Research Program

S. Scott 1), A. Bader 2), M. Bakhtiari 3), N. Basse 4), W. Beck 2), T. Biewer 5), S. Bernabei 1), P. Bonoli 2), B. Bose 2), R. Bravenec 6), I. Bespamyatnov 6), R. Childs 2), I. Cziegler 2), R. Doerner 7), E. Edlund 2), D. Ernst 2), A. Fasoli 8), M. Ferrara 2), C. Fiore 2), T. Fredian 2), A. Graf 9), T. Graves 2), R. Granetz 2), N. Greenough 1), M. Greenwald 2), M. Grimes 2), O. Grulke 10), D. Gwinn 11), R. Harvey 12), S. Harrison 3), T. C. Hender 13), J. Hosea 1), D. F. Howell 13), A. E. Hubbard 2), J. W. Hughes 2), I. Hutchinson 2), A. Ince-Cushman 2), J. Irby 2), T. Jernigan 5), D. Johnson 2), J. Ko 2), P. Koert 2), B. LaBombard 2), A. Kanojia 2), L. Lin 2), Y. Lin 2), B. Lipschultz 2), J. Liptac 2), A. Lynn 14), P. MacGibbon 2), E. Marmar 2), K. Marr 2), M. May 15), D. R. Mikkelsen 1), R. McDermott 2), A. Parisot 2), R. Parker 2), C. K. Phillips 1), P. Phillips 6), M. Porkolab 2), M. Reinke 2), J. Rice 2), W. Rowan 6), M. Sampsell 6), G. Schilling 1), A. Schmidt 2), N. Smick 3), A. Smirnov 12), J. Snipes 2), D. Stotler 1), J. Stillerman 2), V. Tang 15), D. Terry 2), J. Terry 2), M. Ulrickson 16), R. Vieira 2), G. Wallace 2), D. Whyte 2), J. R. Wilson 1), G. Wright 3), J. Wright 2), S. Wolfe 2), S. Wukitch 2), G. Wurden 17), H. Yuh 18), K. Zhurovich 2), J. Zaks 2), S. Zweben 1)

- 1) Princeton Plasma Physics Laboratory, Princeton, NJ, USA
- 2) Plasma Science and Fusion Center, Massachusetts Institute of Technology, Cambridge, MA, USA
- 3) University of Wisconsin, Madison, WI, USA
- 4) current address: ABB Corporate Research, Baden-Dättwil, Switzerland
- 5) Oak Ridge National Laboratory, Oak Ridge, TN, USA
- 6) University of Texas, Austin, TX, USA
- 7) University of California, San Diego, CA, USA
- 8) Centre de Recherches en Physique des Plasmas Association EURATOM - Confédération Suisse Ecole Polytechnique Fédérale, Station 13 CH-1015 Lausanne, Switzerland
- 9) University of California, Davis, CA, USA
- 10) MPI for Plasma Physics, EURATOM Association, Greifswald, Germany
- 11) Bagley Associates, Lowell, MA, USA
- 12) CompX, Del Mar, CA, USA
- 13) Euratom/UKAEA Fusion Association, Culham Science Centre, Abingdon, OX14 3DB, UK
- 14) current address: University of New Mexico, XX, NM, USA
- 15) Lawrence Livermore National Laboratory, Livermore, CA, USA
- 16) Sandia National Laboratory, Albuquerque, NM, USA
- 17) Los Alamos National Laboratory, Los Alamos, NM, USA
- 18) Nova Photonics, Inc., Princeton, NJ, USA

email-contact of main author: sscott@pppl.gov

Abstract. Alcator C-MOD has compared plasma performance with plasma facing components (PFCs) coated with boron to all-metal PFCs to assess projections of energy confinement from current experiments to next-generation burning tokamak plasmas. Low- Z coatings reduce metallic impurity influx and diminish radiative losses leading to higher H-mode pedestal pressure that improves global energy confinement through profile stiffness. RF sheath rectification along flux tubes that intersect the RF antenna is found to be a major cause of localized boron erosion and impurity generation. Initial lower-hybrid current drive (LHCD) experiments ($P_{LH} < 900$ kW) in preparation for future Advance Tokamak studies have demonstrated fully noninductive current drive at $I_p \sim 1.0$ MA with good efficiency, $I_{drive} = 0.4P_{LH}/n_{eo}R$ (MA,MW, 10^{20}m^{-3} ,m). Understanding the mechanisms responsible for regulating the H-mode pedestal height is also crucial for projecting performance in ITER. Modeling of H-mode edge fueling indicates high

self-screening to neutrals in the pedestal and scrape-off layer (SOL), and reproduces experimental density pedestal response to changes in neutral source, including a weak variation of pedestal height and constant width. Similar to the scaling of edge pressure gradients in the H-mode pedestal observed previously, pressure gradients in the near SOL of Ohmic L-mode plasmas are observed to scale consistently as I_p^2 , and furthermore show a significant dependence on X-point topology. Fast camera images of intermittent turbulent structures at the plasma edge show they travel coherently through the SOL with a broad radial velocity distribution having a peak at about 1% of the ion sound speed, in qualitative agreement with theoretical models. Fast D_α diagnostics during gas puff imaging show a complex behavior of discrete ELMS, starting with an $n \approx 10$ precursor oscillation followed by a rapid primary ejection as the pedestal crashes and then multiple, slower secondary ejections. The potential to mitigate disruptions in ITER through massive gas-jet impurity puffing has been extended to significantly higher plasma pressures and shorter disruption times. The fraction of total plasma energy radiated increases with the Z of the impurity gas, reaching 90% for krypton. A Phase Contrast Imaging diagnostic has been used to study the structure of Alfvén cascades and turbulent density fluctuations in plasmas with an internal transport barrier.

1 Introduction

Recent research on the high-field, high-density diverted Alcator C-MOD tokamak has focussed on the plasma physics and plasma engineering required for ITER and for attractive fusion reactors. C-MOD is prototypical of ITER in several key respects including toroidal magnetic field, equilibrated ions and electrons, plasma density, power density in the scrape off layer (SOL), low momentum input, high- Z plasma facing components (PFCs), divertor neutral opacity and long pulse length compared to the skin time. Recent experimental campaigns have focused on understanding the physical mechanisms that affect the plasma performance realized with all-molybdenum walls versus walls with low- Z coatings. Detailed measurements of the temperature and density profiles in the near SOL and fast framing movies of the turbulent structures provide improved understanding of the mechanisms that control transport in the edge region, which is crucial for projecting the performance of ITER. Disruption mitigation via massive gas-jet impurity puffing has proven successful at high plasma pressure, indicating this technique has promise for implementation on ITER.

2 Performance with all-metal walls versus low- Z coatings

Tungsten has been selected as the primary material for PFCs in ITER and fusion reactors based on its low tritium retention, low erosion rate, and low neutron damage rate. High- Z metallic PFCs including molybdenum and tungsten have hydrogen recycling and radiative properties that differ substantially from low- Z PFCs (carbon, beryllium) and low- Z PFC coatings (boron, beryllium, lithium). Most of the world's divertor and confinement database has been developed in tokamaks with low- Z PFCs or low- Z PFC coatings, but carbon has been relegated to a small fraction of the PFC surfaces in ITER and none in a high-fluence demonstration reactor.

Until recently, the PFC environment in C-MOD has been molybdenum coated with a thin layer of boron, plus boron-nitride protective tiles near the RF antennas. The boron layer is replenished periodically using a low-temperature electron cyclotron plasma discharge fueled with diborane gas. This 'boronization' process is typically carried out overnight, depositing about 200 nm of boron over a period of 10-12 hours, and the resonance location can be swept from the inner wall to beyond the outer limiters by scanning the toroidal field. The deposition location can also be localized radially by imposing a

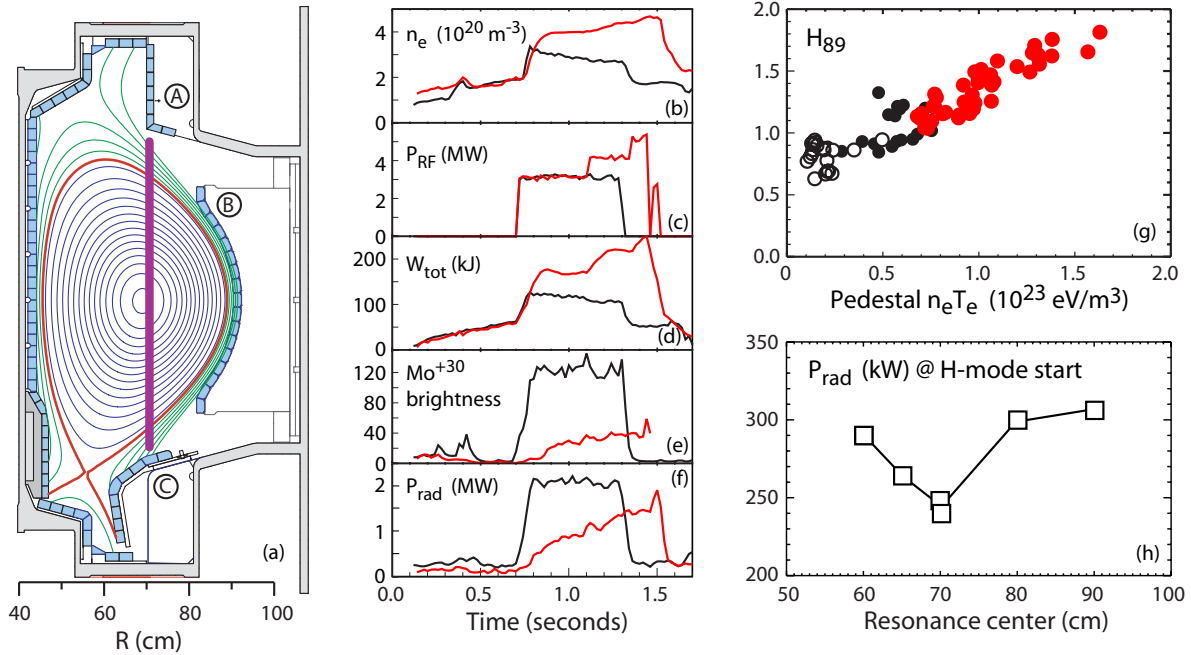


Figure 1: (a) Optimized boronization resonance deposits boron onto upper gusset tiles (A) and lower outer divertor (C). (b-f) Comparison of plasma performance with (red) and without boron (black) coating. (g) Energy confinement parameter H_{89P} as a function of pedestal pressure with (red) and without (black) boron coating. (h) Radiated power shortly after L-H transition as a function of boron deposition, showing optimum location at $R \approx 70$ cm.

small variation in toroidal field. Prior to the 2005 experimental campaign, boron was removed from all PFCs and the boron nitride tiles were replaced with molybdenum tiles to allow a direct comparison of plasma performance with and without a boron coating, yielding a surface concentration of 80-90% Mo with 10-20% residual B. H-mode plasmas were readily obtained during RF heating with pure Mo (i.e. uncoated) PFCs, but the impurity concentration was high ($n_{Mo}/n_e \leq 0.1\%$), radiated power was high, and energy confinement was degraded, with $\tau_E = 0.9 - 1.3 \times \tau_{E89P}$ [1]. This was due to local cooling of the pedestal by Mo radiation (the dominant radiator in C-MOD) which lowers the pedestal pressure and propagates to lower plasma core pressures and global stored energy through profile stiffness (Fig. 1g). After applying boron coatings n_{Mo}/n_e was reduced by a factor of 10-20 with H_{89P} approaching 2. The boronized discharge illustrated in Fig. 1(b-f) obtained a world-record volume averaged plasma pressure ($\langle p \rangle = 1.8$ atm) at $\beta_n = 1.74$. The beneficial effects of overnight boronization last 20-50 high-power discharges, with radiated power rising monotonically shot-to-shot and with reduced τ_E visible after about 50 MJ of total deposited energy in ICRF-heated discharges.

A body of evidence suggests that the boron erosion is spatially localized: prior to the 2005 campaign vessel cleaning, boron layers averaging 6000 nm thick were measured on a poloidal array of tiles, indicating that the majority of PFC surfaces experienced little boron erosion. By contrast, the outer divertor surfaces extending from the bottom of the outer divertor vertical section to $R \approx 0.67$ m showed the highest Mo surface concentrations (10-50%), presumably due to net erosion of the boron layers by the high particle and heat fluxes to those surfaces. Brief, between-discharge boronization (BDB) has been utilized as a diagnostic of the erosion location. A thin (10-nm) boron layer was applied locally

in major radius as the resonance was swept ± 5 cm. The layer eroded in just 1-2 shots, allowing controlled studies of the boron effectiveness. Figure 1h illustrates that there is a pronounced optimum location for boron deposition at $R \approx 70$ cm, suggesting that replenishing the boron layer at the top of the outer divertor and the upper gusset tiles is particularly important (Fig. 3a).

RF sheath rectification: Recent experiments suggest that both boron erosion and Mo impurity generation are strongly affected by RF sheath-rectification along flux tubes that intersect with or pass in front of the RF antenna[2]. These flux tubes intersect the upper part of the outer limiters, upper gusset tiles and the top of the outer divertor, precisely where little boron accumulation was observed. Controlled studies with BDB show that RF-heated plasmas suffer increased radiation after just a single shot while Ohmic H-mode plasmas with comparable total energy input experience increased radiation only after 4-6 shots, suggesting that RF waves themselves rather than just total energy/particle fluence to the PFCs are important in the erosion mechanism. This conjecture was convincingly demonstrated by depositing a thin layer of boron with BDB followed by a series of RF-heated plasma discharges without further boron deposition. Performance degradation was observed on the second discharge if the same RF antenna was used but not if a different RF antenna was used on the second shot, proving that each antenna is associated with a different erosion location.

Deuterium Retention: Following ultrasonic cleaning of PFC tiles, deuterium retention was measured in a series of six Ohmic, non-disruptive plasmas in a predominantly high-Z PFC environment. Low deuterium retention of order 0.1% was expected in Mo on the basis of previous measurements using ion beams incident on Mo target samples[3], but surprisingly the fraction of injected gas retained in the C-MOD vessel surfaces was $\sim 45\%$ in the first discharge, decreasing to a quasi-steady-state value of $\sim 30\%$ by the end of the shot sequence. Similar retention values were observed on boronized PFCs. Measurements of deuterium retention and depth profile during low-temperature plasma bombardment of a pure Mo target in the Dionisos facility[4] also indicate unexpectedly high levels of retained deuterium ($\sim 0.25\%$ of incident flux retained; surface atomic ratio D/Mo $\sim 1\%$) and deep deuterium penetration (≥ 5000 nm). A candidate mechanism for apparent discrepancy between retention measurements with high energy (~ 5 keV) ion beams versus low energy, high-flux plasma is that the plasma generates D trapping sites at the surface that migrate into the bulk.

3 Lower hybrid current drive

A major goal of the C-MOD program is achieving high performance advanced-tokamak plasmas with up to 1 MA non-inductive current (70% bootstrap, 30% LHCD) at high confinement ($H_{89p} \approx 2.5$) and high normalized beta ($\beta_n \leq 3$), and sustaining this performance for several current relaxation times. An objective of the lower hybrid program is to provide information for the decision on installing LHCD capability on ITER and to support advanced tokamak physics research. The C-MOD LHCD system comprises 12 klystron tubes with 3 MW total source power, a rear and front waveguide assembly, and a 4 x 24 plasma-facing waveguide coupler. A unique feature of the system is its capability to vary the launched n_{\parallel} spectrum over the range $n_{\parallel} = 1.5 - 4.5$ on a rapid time scale (~ 1 ms), thereby providing control of the radial location of driven current. The original coupler fabricated from a titanium alloy suffered serious and rapid erosion when exposed

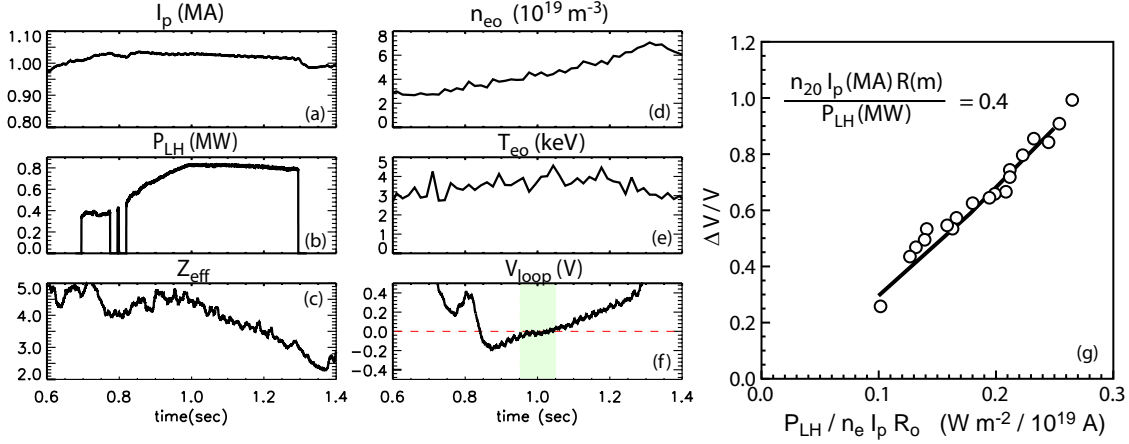


Figure 2: (a-f) Waveforms of conditions in discharge with ~ 1 MA current driven by LHCD. Shaded green region represents ~ 100 ms interval with near-zero loop voltage. (g) Analysis of current drive efficiency in a lower hybrid power scan at $n_{\parallel} = 1.6$, $P_{LH} = 120 - 830$ kW, $I_p = 0.7 - 1.0$ MA, and $\bar{n}_e = 3.5 - 7.0 \times 10^{19} \text{ m}^{-3}$.

to C-MOD plasmas by an as-yet undetermined mechanism. In 2006 it was replaced by a stainless steel coupler which has functioned well, with no surface erosion and only minor melting observed on the edge waveguides after a full 14 week run campaign.

The first lower hybrid experimental campaign was limited to L-mode plasmas without ICRF heating at modest density. Initial results are quite encouraging: over 900 kW of power have been coupled to C-MOD plasmas with a coupling efficiency that is consistent with code predictions[5] when the effect of a small (~ 1 mm) assumed vacuum gap is included[6]. As shown in Fig. 2, 800 kW of coupled LH power drove the surface loop voltage negative or near zero for approximately 100 ms ($\approx \tau_{CR}$) in a $I_p = 1.0$ MA plasma at $n_{eo} \approx 4 \times 10^{19} \text{ m}^{-3}$, consistent with current-drive efficiency calculations by the GENRAY-CQL3D[7] model. The loop voltage increased later on in the discharge as the density rose to $7 \times 10^{19} \text{ m}^{-3}$ thereby decreasing the driven current below 1 MA. We have also observed sawtooth stabilization at $I_p = 700$ kW, $\bar{n}_e = 4.4 \times 10^{19} \text{ m}^{-3}$ with $P_{LH} \approx 750$ kW that indicates significant off-axis current drive. The central electron temperature increased from 2.6 to 3.7 keV due to the combined effects of electron heating by the LH waves and cessation of the sawteeth. Overall, the energy confinement during LH heating appears to be consistent with that of low density Ohmic, and no unusual impurity influx is observed. The hard x-ray spectrum measured with a 32-chord perpendicular x-ray camera becomes more energetic and the emissivity profile broadens as n_{\parallel} is reduced from 3.1 to 1.6, in qualitative agreement with model expectations.

We applied the method developed by Giruzzi[8] to assess the current drive efficiency in plasmas for which the loop voltage does not go to zero. The fractional change in loop voltage, $\Delta V/V$ was measured in a lower hybrid power scan at fixed plasma density and current. The current drive efficiency inferred from this analysis (Fig. 2g) is at the upper end of the range expected theoretically, ($I_{drive} = 0.4 P_{LH} \text{ (MW)} / n_{eo} (10^{20} \text{ m}^{-3}) R \text{ (m)}$). The coefficient is 0.28 if \bar{n}_e rather than n_{eo} is used as the density normalization.

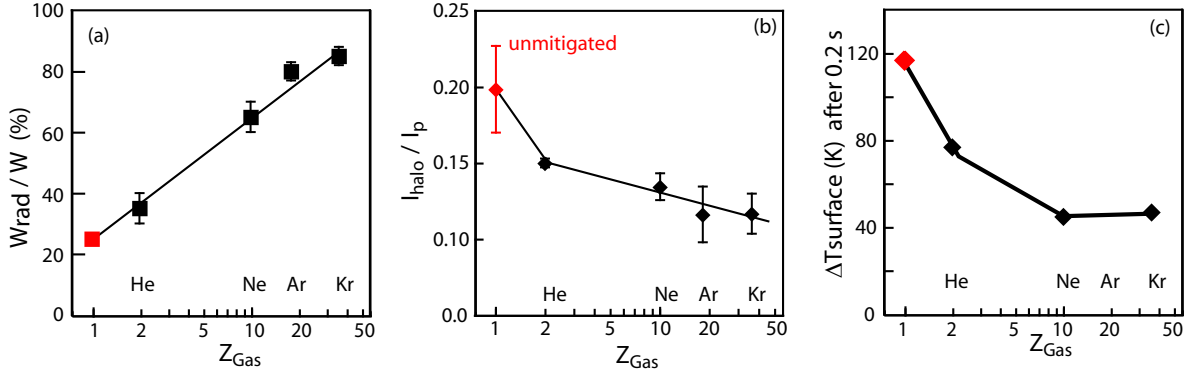


Figure 3: (a) Normalized halo current versus atomic number of mitigating gas; (b) fraction of total power radiated during the disruption; (c) rise in surface temperature at the outer lower divertor surface following disruption.

4 Disruption Mitigation

Disruption-induced damage arising from high power loads on divertor surfaces, generation of large relativistic electron runaway currents, and electromagnetic loads on conducting structures due to halo currents are major concerns for ITER and tokamak reactors. The technique of disruption mitigation through massive gas-jet impurity puffing originally developed on DIII-D [9] has been extended to significantly higher plasma pressures and shorter disruption times. An ORNL fast-response valve delivered short, massive puffs of helium, neon, argon, or krypton gas to a delivery nozzle near the outer plasma edge. As shown in Fig. 3a, the fraction of total plasma energy radiated increased with Z of the impurity gas, reaching 90% for krypton[10]. The increased radiated power cools the plasma during the current quench and additionally the impurity increases Z_{eff} , both of which decrease the L/R quench time. Consequently, the disruption-mitigated plasma has less time to move vertically before contacting the torus wall, thereby reducing the disruption halo currents by up to $\sim 50\%$ (Fig. 3b). Infrared camera images of the outboard divertor tiles show less surface heating in mitigated disruptions (Fig.3c), consistent with the loss of most of the plasma energy to isotropic radiation. Studies of disruption mitigation with mixtures of helium and argon show promise in combining the favorable radiative properties of a high- Z gas with the rapid transit of helium through the gas delivery system, which is limited by its thermal speed.

High speed imaging of the gas jet plumes show that impurity neutrals do not penetrate deeply into the plasma and initially cool just the periphery of the plasma. Nevertheless, within a few hundred microseconds some impurity ions appear in the plasma core and the core temperature decreases on the same time scale. NIMROD MHD simulations indicate that the initial edge cooling triggers rapid growth of 2/1 and 1/1 tearing modes resulting in a large stochastic region that mixes impurity ions into the core[11].

5 Scaling of the locked-mode threshold

A major uncertainty for projecting the error field threshold for locked modes on ITER is its scaling with major radius. The error field scaling is typically represented as a power law, $B_{err}/B_t \propto n^{\alpha_n} B^{\alpha_B} q^{\alpha_q} R^{\alpha_R}$. Dimensional scaling imposes the constraint $\alpha_R = 2\alpha_n + 1.25\alpha_B$

and experiments have established that $\alpha_n = 1$, thus a knowledge of the scaling with toroidal field (α_B) also determines the scaling with machine size. Unfortunately, scaling experiments in C-MOD, JET, DIII-D, and COMPASS-D have yielded disparate values of α_B . C-MOD executed a controlled toroidal field scan at fixed plasma shape (lower single null), fixed $q_{95} = 3.5$, $n/n_G = 0.18$. On each discharge, the error field imposed by external coils (predominantly $m/n = 1/1, 2/1$ with small $3/1$ component) was ramped in magnitude until a locked mode was identified from cessation of sawteeth and an $n = 1$ magnetic signature. As shown in Fig. 4 the data are well fit by $\alpha_B = -1.06 \pm 0.15$ which implies a major-radius scaling $\alpha_R = 0.68 \pm 0.19$ that extrapolates to a favorable threshold $\tilde{B}_{21}/B \approx 0.9 \times 10^{-4}$ in ITER at its ohmic target plasma density ($2 \times 10^{19} \text{m}^{-3}$).

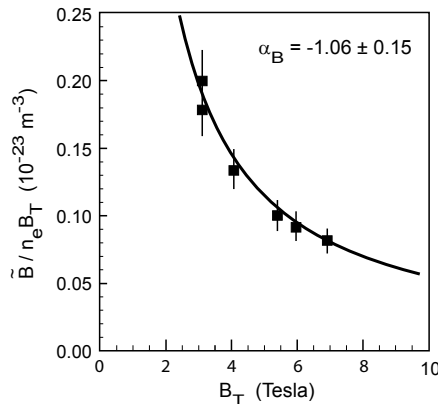


Figure 4: *Scaling of error field required for mode-locking as a function of B_T .*

6 Alfvén Cascades

The phase contrast imaging system (PCI)[12] and the magnetic pick-up coils are being used on Alcator C-Mod to study the physics of Alfvén eigenmodes. Of particular interest are the Alfvén Cascades, core-localized modes that exist in reversed-shear plasmas. These modes can be driven by the fast ion population from hydrogen minority ion cyclotron heating and are very sensitive to small changes in the minimum of the q profile resulting in a frequency chirping as the current diffuses. Modeling with the ideal MHD code NOVA-K[13] is being used to model the frequency characteristics of these modes and infer the evolution of the current profile (Fig. 5). Typical PCI signals from the 32 element detector array show multiply peaked structures for the cascades. Before the development of the ‘synthetic’ PCI tool used with the NOVA-K results, it was unknown whether this was a measurement of a mode with multiple peaks in its radial structure, or an effect arising from the line integration of density fluctuations. First results from NOVA-K using typical eigenmode solutions with a single peak in the radial structure showed a triplet of peaks in the simulated PCI data, matching closely the experimental data. Application of these methods should allow for more accurate modeling of the central safety factor[14].

7 Turbulence measurements and simulations

Nonlinear gyrokinetic simulations of Trapped Electron Mode (TEM) turbulence in C-MOD have moved beyond comparisons with inferred transport fluxes to a more fundamental

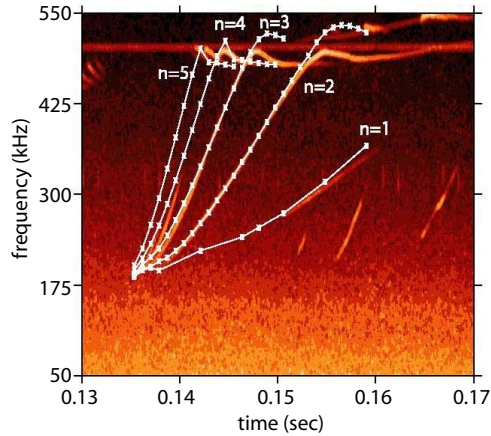


Figure 5: *PCI data is shown in red scale, overlaid are numerical results from NOVA in white. The initial frequency calculated from NOVA matches the experimental data within the uncertainty of the experiment.*

comparison with measured density fluctuation spectra. An internal transport barrier ITB that can be generated in C-MOD with off-axis ICRF heating[15], and regulated with on-axis ICRF heating[16], provides vertical localization along viewing chords of the PCI diagnostic, and an opportunity to study particle transport without sources. Previously, we demonstrated that nonlinear gyrokinetic simulations of Trapped Electron Mode (TEM) turbulence provide a quantitative understanding of internal transport barrier control in Alcator C-MOD, with no adjustable model parameters[17]. Recently, a new synthetic diagnostic[18] was added to the GS2 gyrokinetic code to allow direct comparison with chord-integrated density fluctuations measured along the 32 PCI chords. There is excellent agreement between the simulated and measured wavelength spectra over the range 1 - 8 cm^{-1} as illustrated in Fig. 6(b). During on-axis heating of the C-MOD ITB, density fluctuations are strongly increased as TEM modes, a primary candidate to explain electron thermal transport, are driven unstable. The relative increase in density fluctuation level with on-axis heating is reproduced by the GS2 simulations, as shown in Fig. 6(a).

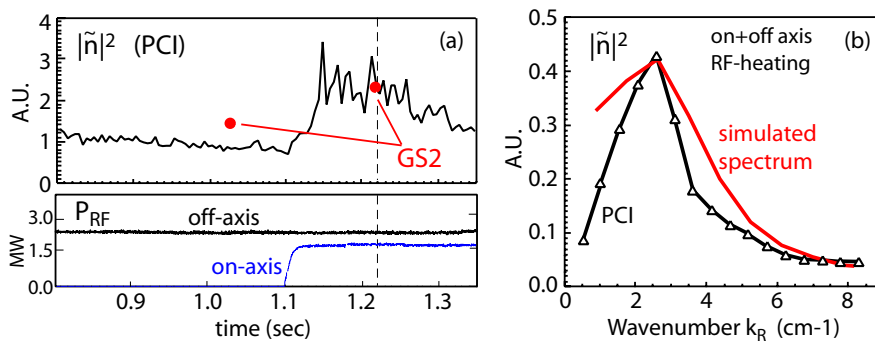


Figure 6: (a) *Time history of chord-integrated density fluctuation level when on-axis ICRF power is applied to a plasma with an internal transport barrier generated by off-axis ICRF heating. Blue points represent the fluctuation level computed by GS2.* (b) *Comparison of measured and simulated k -spectrum at 1.22 sec, when RF provided both on- and off-axis heating.*

8 Pedestal physics

The density and pressure attained in the H-mode pedestal remains a key uncertainty in performance projections for ITER and physics-based models are needed for reliable extrapolation from existing tokamaks. Previous studies[19] demonstrated that the H-mode pressure gradient (∇p_e) obeys an I_p^2 scaling with a numerical coefficient that depends on collisionality. Recent work has focused on extending the empirical scaling of pedestal height and widths over a wider parameter range and clarifying our understanding of the roles played by both plasma transport processes and neutral fuelling on pedestal structure[20]. Over the range $I_p = 0.4 - 1.5$ MA and $B_T = 2.7 - 6.3$ Tesla, we observe a nearly linear scaling of edge pedestal density with current with little systematic B_T dependence (Fig. 7a). The robust dependence on a single plasma parameter that is irrelevant to neutral-plasma interactions suggests that the density pedestal is largely defined by plasma transport mechanisms, and not solely by edge particle fuelling. In H-mode plasmas there is typically no gas feed and the density is sustained entirely by wall recycling, and experiment shows a weak dependence of $n_{e,ped}$ on line-averaged density prior to the L-H transition. This trend is illustrated in Fig. 7b, in which the H-mode pedestal density increases 30-40%, for a factor-of-two variation in n_{eL} consistent with a previously inferred scaling: $n_{e,ped} \propto n_{eL}^{0.4}$.

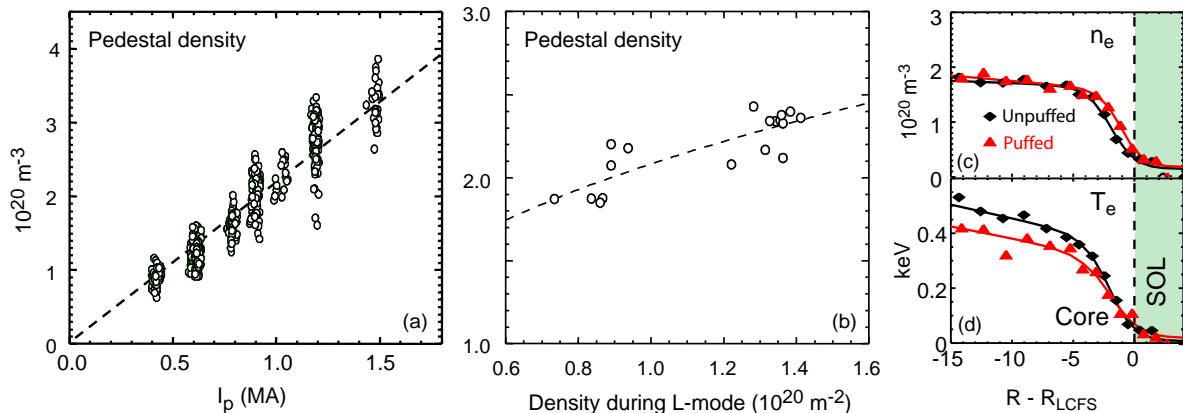


Figure 7: (a) Scaling of pedestal density with I_p . (b) Scaling of pedestal density with density in preceding L-mode phase. (c,d) Edge Thomson scattering profiles of electron density and temperature in 0.81 MA H-mode plasma before and during aggressive D_2 puffing at the inner wall. The density pedestal shifts radially outward but the height remains essentially unchanged.

The empirical scaling of the pedestal density width Δ_n is considerably different on C-MOD versus DIII-D, with C-MOD observing no dependence of Δ_n on $n_{e,ped}$ while DIII-D observes $\Delta_n \propto n_{ped}$, the latter being consistent with simple 1D fluid modeling that invokes a radial flux balance between ions and neutrals. A kinetic treatment of neutral transport using the KN1D code reproduces the fundamental C-MOD trends[20]: as fuelling is increased, the modeled ion density increases weakly while the pedestal width remains roughly constant. Effectively, the increased density causes a greater fraction of the ionization to occur near or outside the foot of the pedestal, leading to a ‘self-screening’ pedestal. This mechanism is clearly demonstrated by strong (tens of T-l/s) gas puffing into an H-mode plasma (Fig. 7(c-d)), whose density pedestal moves outward slightly but does not change in magnitude. The SOL in ITER is expected to be similarly opaque to neutrals,

and so these results suggest there may be only limited capability to control the density pedestal height in ITER through gas feed.

9 Scrape-off layer phase space

Previous analysis [21] of scanning Langmuir-Mach probe data showed that pressure gradients in the SOL of Ohmic L-mode discharges scale as I_p^2 (similar to the scaling of edge pedestal pressure in H-mode plasmas) and that the pressure gradients clamp at similar values of the MHD ballooning parameter $\alpha_{MHD} = q^2 R \beta / L_{pe}$ when the normalized collisionality parameter ($\alpha_d \propto \lambda_e^{1/2} / (q R^{3/4} L_{\perp}^{1.4})$) is held fixed. Over a wide range in machine parameters B_T , I_p , and \bar{n}_e , the observed SOL states are observed to cluster around a narrow band in the two-dimensional space (α_{MHD}, α_d) as would be expected from electromagnetic fluid drift turbulence (EMFDT). Comparing probe measurements on the low and high-field SOLs revealed that the observed large SOL flows are caused by ballooning-like transport that dumps larger particle fluxes into the low-field region, thereby generating a density imbalance that drives a helical flow in the SOL toward the high-field side. Recent density scans with $0.1 < n/n_G < 0.5$ over an extended range of I_p and B_T (0.4-1.1 MA, 2.7-5.8 T) have focussed on the effect of the X-point topology on the SOL pressure gradients [22]. As shown in Fig. 8a, the SOL pressure gradients continue to scale consistently as I_p^2 , but with a numerical value that depends on the X-point topology, with higher gradients attained in the LSN configuration. For a given X-point configuration, data from different plasma currents collapse into a narrow band when plotted in EMFDT phase space (confirming the dominant I_p^2 scaling), but the LSN and USN datasets form two separate bands, with lower null achieving higher values of α_{MHD} (Fig. 8b). As illustrated in Fig. 8c, the SOL plasma flows are dramatically different in the LSN versus USN configurations, and the range of collisionality parameter α_d where the LSN obtains higher α_{MHD} corresponds to the region where there is a significant difference in the parallel Mach number on the low-field side. This indicates that co-current flows in the SOL are associated with higher pressure gradients, and suggests that flow is another controlling variable in the EMFDT phase space ($\alpha_{MHD}, \alpha_D, M$). Recent experiments with reversed B_T and I_p in USN plasmas confirm these results.

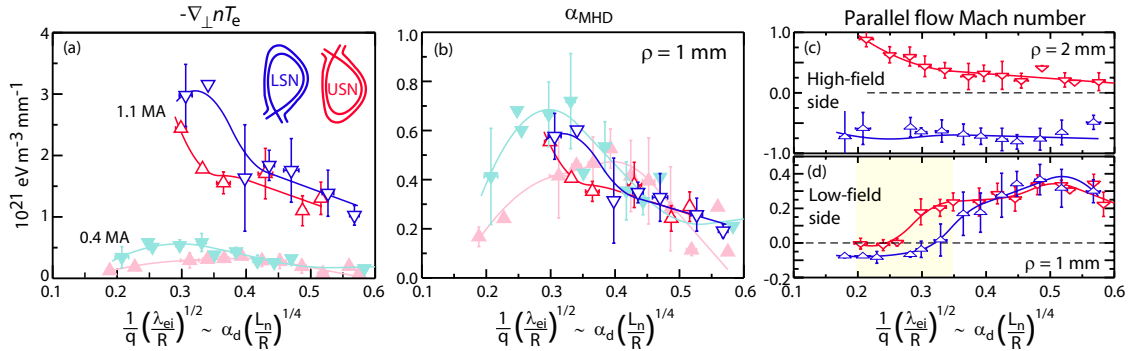


Figure 8: (a) Electron pressure gradients in the edge scale dominantly with I_p^2 resulting in (b) similar values of α_{MHD} when the local collisionality is the same. (c) Near-sonic parallel flows on the high-field side change direction in going from LSN to USN. (d) Parallel flows on the low field side tend to be less co-current directed in USN over the collisionality range where α_{MHD} is also lower (flow data are averaged over $I_p = 0.4, 0.8$ and 1.1 MA).

10 GPI Turbulence imaging

Electrostatic turbulence in the SOL of C-MOD has been measured [23] using 1-D and 2-D gas puff imaging (GPI) and Langmuir probes. The cross-correlation between light fluctuations seen by the 1-D GPI (δI) and the density (δn) and ($\delta\phi$) potential fluctuations seen in the Langmuir probe was measured by aligning the two diagnostics with a parallel separation of 3 m along the same magnetic field line in the SOL. The cross-correlation between ($\delta I, \delta n$) was maximum when the two diagnostics were on the same field line, but the cross-correlation between ($\delta I, \delta\phi$) showed a poloidal dipole structure centered on the field line, in qualitative agreement with the blob model for edge turbulence structures ([24], [25]). The radial and poloidal velocity distribution of the blob structures in the SOL was directly measured using the 2-D GPI imaging system, as shown in Fig. 9. Ninety percent of the structures are seen to propagate radially outward with a most probable speed of ~ 500 m/sec, or about 1% of the local ion sound speed. The magnitude of this speed is roughly comparable to that predicted by models of blob propagation in the SOL.

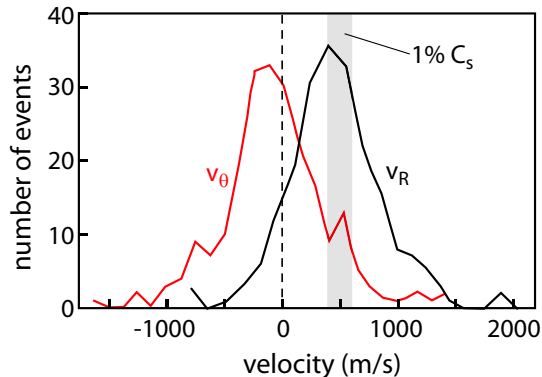


Figure 9: Frequency distribution of velocity for large-amplitude fluctuation structures inferred from fast camera GPI images. The shaded area represents 1% C_s in the mid-to-far-SOL ($\rho = 10 - 20$ mm).

11 ELMs

The standard H-mode regime in C-MOD is Enhanced D_α [26] in which a quasi-coherent mode localized in the pedestal region increases particle transport and thereby avoids excessive impurity and pressure build-up that trigger discrete ELMs or radiative collapse. Recently, a new region of H-mode operational space at low collisionality ($\nu^{ped} < 1$) and high triangularity ($\delta > 0.75$) has been accessed where discrete, relatively large ELMs are present [27]. These ELMs do not destroy the temperature or density pedestal, and the energy loss per ELM is typically 10-20% of W_{ped} . Their structure and evolution have been studied using magnetics and D_α emission from GPI. The emissions from outboard vertical and radial arrays of views and from an inboard radial array are analyzed. A complex time history is observed, with a 200-400 kHz, $n_{toroidal} \sim 10$ precursor oscillation starting inside the separatrix, followed by the ejection of rapidly propagating ($v_R = 0.5 - 8.0$ km/s) primary filaments (Fig. 10). The primary ejection into the outboard SOL is coincident

with the onset of a short-lived 0.5-1 MHz magnetic oscillation. This initial evolution is followed by multiple slower secondary filament ejections.

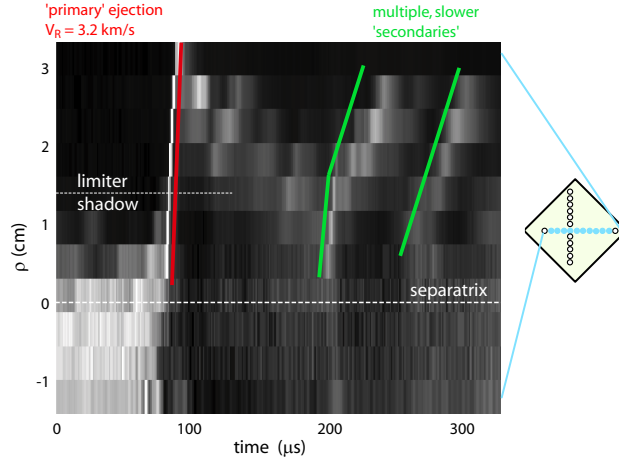


Figure 10: *Structure of primary and secondary ejections during discrete ELMs as measured by a radial array of views at the plasma edge on the low-field side.*

12 Facility Upgrades and Future Plans

Over the next two years, a number of facility upgrades on C-MOD will enhance its capability to study advanced tokamak (AT) plasma regimes and ITER-relevant physics and engineering issues. A toroidal cryopump is now being installed on the inboard side of the upper divertor chamber to provide active density control needed to reduce the density to values consistent with efficient LHCD. Initial test-stand performance has demonstrated pumping speeds of 10^4 l/s for deuterium gas, which is sufficient to deplete the C-MOD particle inventory several times per plasma discharge. A second Lower Hybrid launcher will be installed to increase the power capability to 4 MW (source power), and a new 4-strap RF antenna will replace two of the existing 2-strap antennas with no net change to the total RF power capability. The ICRF system will be upgraded with fast ferrite tuners to allow one antenna to tune through changes in plasma configuration and ELMs on a 1 ms time scale. Based on the promising results of tungsten brush tiles in the lower divertor this run campaign (no evidence of significant tungsten emission), a complete toroidal ring of tungsten tile modules will be installed in the lower divertor based on an improved ‘lamallae’ design. The long-pulse diagnostic neutral beam is being rotated from its current orientation (exactly perpendicular to the toroidal field) 7° in the toroidal direction to eliminate a population of ripple-trapped fast ions that confuses the calibration of the MSE diagnostic. A number of extensive diagnostic upgrades are also in progress, including an imaging x-ray crystal spectrometer for fine-scale profile measurements (~ 40 spatial chords) of T_i and v_ϕ , PCI upgrades to extend its measurement capability to $k \sim 60 \text{ cm}^{-1}$, a swept-frequency reflectometer to measure the density fluctuation correlation length at $2 \times 10^{20} \text{ m}^{-3}$, a second fast-framing GPI camera to view the lower divertor, a 20-channel polarimeter to supplement the MSE q -profile measurements, and installation of ‘marker’ tiles to improve our understanding of the localization of impurity sources.

This work is supported by Department of Energy Coop. Agreements DE-FC02-99ER54512 and DE-FC02-04ER54698, Grants DE-FG02-04ER54758 and DE-FG02-04ER54762, and

Contracts DE-AC02-76CH03073 (PPPL), DE-AC05-00OR22725, W-7405-ENG-48, W-7405-ENG-36, and USDOE Grant DE-FG03-96ER54373.

References

- [1] LIPSCHULTZ, B., et al., Phys. Plasmas **13** (2006) 056117.
- [2] WUKITCH, S., et al., 17th PSI conference, Hefei, China, 2006, submitted to J. Nucl. Mater.
- [3] CAUSEY, R., et al., J. Nucl. Mater. **266-269** (1999) 467.
- [4] WRIGHT, G.M., et al., 17th PSI conference, Hefei, China, 2006, submitted to J. Nucl. Mater.
- [5] BRAMBILLA, M., Nucl. Fusion **16**, (1976) 47.
- [6] LIPTAC, J.E. , Doctoral Thesis, Dept. of Nuclear Science and Engineering, MIT, May, 2006.
- [7] HARVEY, R.W., McCOY, M.G., Proceedings of the IAEA Technical Committee Meeting on Advances in Simulation and Modeling of Thermonuclear Plasmas, Montreal, 1992, p. 489-526, IAEA, Vienna (1993).
- [8] GIRUZZI, G., et al., Nucl. Fusion **37** (1997) 673.
- [9] WHYTE, D. G., et al, Phys. Rev. Lett. **89** (2002) 055001.
- [10] GRANETZ, R., et al., this conference, EX/4-3.
- [11] IZZO, V., et al., this conference, TH/P3-15.
- [12] PORKOLAB, M., et al., IEEE Transactions on Plasma Science, **34**, 229-334, April 2006.
- [13] CHENG, C.Z. CHANCE, M.S., J. Comp. Phys **71**, (1987) 124.
- [14] PORKOLAB, M., et al., this conference, EX/P6-16.
- [15] RICE, J. E., et al., Nucl. Fusion **41** (2001) 277.
- [16] WUKITCH, S. J., et al., Phys. Plasmas **9** (2002) 2149 and RICE, J. E., Nucl. Fusion **42** (2002) 510.
- [17] ERNST, D. R. et al., Phys. Plasmas **11** (2004) 2637.
- [18] ERNST, et al., this conference TH/1-3; A. Long and D. R. Ernst, Bull. Am. Phys. Soc. **50**(8) GP1.48 (2005) 153.
- [19] HUGHES, J. W., et al., Phys. Plasmas **9** (2002) 3019.
- [20] HUGHES, J. W., et al., Phys. Plasmas **13** (2006) 056103.

- [21] LABOMBARD, B., et al., Nucl. Fusion **45** (2005) 1658.
- [22] LABOMBARD, B., et al., submitted to J. Nucl. Mater. (2006).
- [23] GRULKE, O., TERRY, J.L., LABOMBARD, B., ZWEBEN, S.J., Phys. Plasmas **13** (2006) 102306.
- [24] MYRA, J.R., D. DIPPOLTO, D., Phys. Plasmas **12** (2005) 092511.
- [25] GARCIA, O.E., et al., Phys. Plasmas **12** (2005) 090701.
- [26] GREENWALD, M., et al., Phys. Plasmas **6** (1999) 1943.
- [27] TERRY, J. L., et al., 17th PSI conference, Hefei, China, 2006, to be published in J. Nucl. Mater. (2007).